Macromolecules
ARTICLE

Morphologies of Self-Organizing Regioregular Conjugated Polymer/Fullerene Aggregates in Thin Film Solar Cells

Mao-Yuan Chiu,[†] U-Ser Jeng,[‡] Ming-Shin Su,[†] and Kung-Hwa Wei*,[†]

[†]*Department of Materials Science and Engineering, National Chiao Tung University, 1001 Ta Hsueh Road, Hsinchu 30050, Taiwan, ROC and* [‡]*National Synchrotron Radiation Research Center, 101 Hsin-Ann Road, Science-Based Industrial Park, Hsinchu 30077, Taiwan, ROC*

ABSTRACT: In this study, we used simultaneous synchrotron grazing incidence X-ray scattering and diffraction to elucidate the overall morphologies of bulk heterojunction (BHJ) thin film (ca. 100 nm) solar cells containing phase-separated poly(3-hexylthiophene) (P3HT) and [6,6]-phenyl-C_{61}-butyric acid methyl ester (PCBM) domains. Specifically, the dimensions and orientation of the P3HT crystallites and the sizes of the PCBM aggregates in BHJ thin films were determined. The appropriate PCBM aggregate size and density required for an optimum performance of the film in the photovoltaics device resulted in deteriorated ordering in the out-of-plane direction, but improved the in-plane packing of the P3HT lamellae. When the P3HT crystallites and PCBM aggregates had comparable domain sizes and number densities, the interpercolated networks for electron- and hole-transport were optimized in the film. This new understanding of the underlying mechanism of carrier mobility in BHJ thin films might be crucial in improving the efficiency of future solar cells.

Introduction

The self-organization of conjugated polymers for use in thin film organic optoelectronic devices is an active area of investigation because the in-plane charge mobility can vary greatly depending on the orientation of the polymer crystallites.[1,2] The morphology of the active layer of a bulk heterojunction (BHJ) thin film solar cell containing donor and acceptor units is very critical to the device performance because these phase-separated domains provide percolated pathways for vertical carrier transport to the respective electrodes. Polymer BHJ solar cell devices featuring conjugated polymers and nanoparticles as donors and acceptors, respectively, allow the carriers to be dissociated from excitons upon illumination.[3−6] For example, BHJ solar cells incorporating regioregular poly(3-hexyl thiophene)(P3HT)[7−9] or other polymeric materials[10−17] and [6,6]-phenyl-C_{61}-butyric acid methyl ester (PCBM) can provide power conversion efficiencies (PCEs) of up to 6%.

The packing of regioregular P3HT molecules in BHJ thin film solar cells has been probed extensively using grazing-incidence X-ray diffraction (GIXRD).[18−23] In contrast, techniques for the analysis of the dispersion and aggregation of PCBM in BHJ solar cells containing P3HT have only recently been developed—e.g., 3D tomography transmission electron microscopy,[24−26] Raman spectroscopy,[27,28] and X-ray photoelectron spectroscopy (XPS).[29] These techniques allow the microstructure of a single component in a binary blend to be elucidated qualitatively. Techniques for studying the mutual interactions between the donor and acceptor units—phenomena that actually govern the final phase separation or morphology—have not been reported previously. We believe that determining the size and orientation of both the donor and acceptor domains in a BHJ device will provide a better understanding of the microstructure of the device and the underlying mechanism of carrier transport. For example,

the connection between the out-of-plane carrier mobility in a thin film BHJ solar cell device and its morphology has yet to be elucidated.

In this study, we used synchrotron-based simultaneous grazing incidence small-angle X-ray scattering (GISAXS) and wide-angle X-ray diffraction (GIWAXD) to examine the self-organization of regioregular P3HT and PCBM aggregates, respectively, in a thin film (ca. 100 nm) BHJ device. The GISAXS and GIWAXD can provide statistically averaged morphologies over large areas (ca. mm^2) relative to other imaging techniques that only analyze nanometer-scale phase separation areas locally (ca. μm^2).[30] We also manifested the relationship between the morphology and the out-of-plane charge mobility, which we determined using a space-charge-limited current (SCLC) model.

Experimental Section

Device Preparation and Performance Measurement. A solution of P3HT (M_w 35 000 g/mol, Rieke Metals) in chlorobenzene and blended with a solution of PCBM (Nano-C, Inc.) in chlorobenzene, at P3HT:PCBM blend weight ratios of 1:0, 1:0.6, 1:0.8, 1:1, and 1:1.2, corresponding to PCBM weight percentages of 0, 38, 44, 50, and 55%, respectively. The ITO-coated glass substrate was cleaned through ultrasonic treatment in detergent, methanol, acetone, and isopropyl alcohol; it was then dried in an oven overnight. PEDOT:poly(styrenesulfonate) PSS (Baytron P VP A1 4083) was spin-coated on the ultraviolet ozone−treated ITO and annealed at 140 °C for 20 min in air and then transferred to a glovebox. The P3HT/PCBM blend solutions were spin-coated on top of the PEDOT:PSS layers. The thickness of each film was ca. 100 nm (AFM). Finally, the Al electrode (100 nm) was deposited on the P3HT/PCBM layer under high vacuum (ca. 5×10^{-7} torr) using a thermal evaporator. Hole-only devices, used to investigate hole transport in P3HT/PCBM, were fabricated following the same procedure described above, except that the top electrode was replaced with gold (Au, ca. 100 nm). Electron-only devices were fabricated by

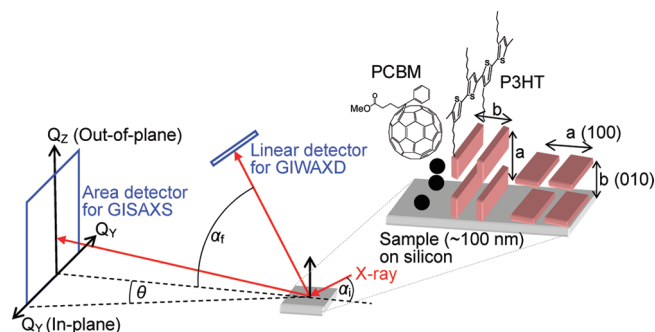*Corresponding author. E-mail: khwei@mail.nctu.edu.tw.

Figure 1. Schematic representation of the GISAXS and GIWAXD setup. The cartoon illustrates the respective orientations of the P3HT crystallites and the PCBM aggregates. Q_Z denotes X-ray scattering in the out-of-plane direction, whereas Q_Y the in-plane direction. The grazing incidence and exit angles are denoted by α_i and α_f, whereas the in-plane scattering angle θ. The linear detector for GIWAXD is aligned in the scattering plane with $\theta = 0$.

spin-coating the active layer on top of glass/Ag (ca. 100 nm), followed by evaporation of the Al (100 nm) top electrode. The completed devices were placed directly on a digitally controlled hot plate and heated at 150 °C for 15 min. After annealing, the devices were encapsulated in UV-curing epoxy and analyzed under an atmosphere of air.

Current density−voltage characteristics of the devices were measured using a Keithley 236 source measure unit. Solar cell performance was measured using a solar simulator (Newport 66902) under AM1.5G irradiation at an irradiation intensity of 100 mW cm^{-2}. The spectral mismatch factor was calculated by comparing the solar simulator spectrum with the AM 1.5G (ASTM G173) spectrum.

Structure Characterization. GISAXS and GIWAXD measurements were performed at the BL23A SWAXS endstation of the National Synchrotron Radiation Research Center, Hsinchu, Taiwan.[31] The beam diameter of the 10 keV beam was 0.5 mm. A gas-type area detector (200 mm × 200 mm) was used for GISAXS, whereas a linear detector (200 mm) for GIWAXD sits in the scattering plane with the in-plane scattering angle $\theta = 0$ (see Figure 1); the sample-to-detector distances were 1905.5 and 750 mm for the GISAXS and GIWAXD configurations, respectively. For GISAXS, the scattering vectors $Q_Z \equiv 2\pi\lambda^{-1}$ ($\sin \alpha_i + \sin \alpha_f$) and $Q_Y \equiv 2\pi\lambda^{-1} \cos \alpha_f \sin \theta$ were defined by the wavelength λ, the incidence, exit angles α_i and α_f, and θ (see Figure 1) of X-rays. The scattering vectors for GISAXS and GIWAXD were calibrated with standard samples of silver behenate and sodalite, respectively.[31,32] The angle of incidence was 0.26° with an accuracy of 0.005°. The samples were prepared on 3 cm × 3 cm Si substrates through spin-coating of P3HT/PCBM solutions; the film thickness was kept the same for each sample (ca. 100 nm). With the setup such configured, the GIWAXD linear detector can cover the (100) (*a*-axis) and (010) (*b*-axis) reflections of the lamellae and π−π interchain stacking of P3HT orientating in the *z*-direction (Figure 1).[1,33] meanwhile, the GISAXS area detector can take the scattering from the P3HT crystallites and PCBM aggregates, of mesoscale domain sizes, and also cover the low-angle P3HT (100) reflection in the *z*-direction.

Results and Discussion

Figure 2 displays the GISAXS 2D patterns of P3HT/PCBM thin films of various compositions that had been subjected to annealing at 150 °C for 15 min. Figure 2a presents a weak powder-diffraction ring at $|Q| = 0.36$ Å^{-1}, corresponding to the 100 reflection plane of a small amount of randomly oriented P3HT crystallites for the pristine P3HT thin film. The high 100 reflection intensity in the *z*-direction, however, indicates that the 100 plane (i.e, thiophene ring plane) of most of P3HT crystallites

orient along the *z*-direction (see Figure 1). The degree of orientation relative to the *z*-direction is illustrated in the azimuthal angle plot of the power ring reflection (see Supporting Information Figure S2); from which the corresponding mosaic spread that was estimated from the peak width is ca. ± 7°. The correlation lengths (or crystal dimensions) D_Z^{100} and D_Y^{100} of the P3HT crystallites calculated from the widths of the 100 peak ($D_i = 2\pi/\Delta Q$, i = Z or Y, where ΔQ is the half width at half-maximum) in the *z*-direction and *y*-direction (see Figure 2e and 2f) were 23.8 and 7.0 nm, respectively. Figures 2b−d show that the (100) peak only broadened marginally in the Q_Z direction, whereas the spread of the peak in the in-plane direction (Q_Y) decreased dramatically upon increasing the PCBM content to 50%; indicating that the in-plane correlation length, D_Y^{100}, of P3HT increases dramatically. The corresponding correlation lengths for the (100) planes of the P3HT crystallites in the blend films are displayed in Figure 4. Moreover, parts b−d of Figure 2 for the blend films also reveal high scattering intensities near the beam centers, relative to that of the pristine P3HT, which intensified upon increasing the PCBM content (see Figure 2, parts c and d). Presumably, we attribute the increase in the low-Q scattering intensity mainly to the formation of PCBM aggregates.

Figure 3 reveals an additional effect of the PCBM aggregates on the orientation of the P3HT crystallites, as determined from the corresponding GIWAXD spectra; the optimal intensity of the (010) peak, coexisting with the P3HT (300) peak, occurred at PCBM concentrations between 38 and 44%, indicating the existence of some P3HT lamellae oriented in the in-plane direction of the thin film. Additionally, we did not observe crystallization of PCBM in the composite thin films. We attribute the hump located between values of Q of 1.3 of 1.6 Å^{-1}, with a broad maximum at $Q = 1.45$ Å^{-1}, to the PCBM halo; this hump, revealing weak ordering of PCBM, intensifies and sharpens slightly upon increasing the PCBM loading in the blend films. To resolve this peak at $Q = 1.45$ Å^{-1}, we compared the changes in the scattering intensity near the beam center in the GISAXS patterns in Figure 2 to that in the GIWAXD profile in Figure 3 for the P3HT/PCBM films. We found that the scattering intensity and the $Q = 1.45$ Å^{-1} hump have synchronized increase as the amount of PCBM increases. Furthermore, in our previous study,[30] we concluded that the intensified low-Q scattering (GISAXS) for the annealed blend film was due to the aggregation of PCBM. Therefore, we are confident that the increase in the intensity of this broad maximum in GIWAXD is due to the increase in the PCBM concentration in the film.

Figure 4a summarizes the related correlation lengths of the P3HT crystallites and the sizes of the PCBM aggregates as a function of the PCBM concentration in the film, based on the results of the GISAXS and GIWAXD analyses. The presence of the PCBM aggregates significantly improved the in-plane correlation (size) of the P3HT crystallites when the concentration of PCBM was greater than 38%; increasing the content of PCBM aggregates, however, inevitably interrupted and systematically deteriorated the degree of P3HT ordering in the out-of-plane direction, resulting in a smaller correlation length (or ordered domain size). In our previous report,[30] the Guinier approximation was used to obtain the radius of gyration (R_g) of PCBM aggregates from the low-Q scattering data of annealed thin film with 44 wt % loading of PCBM in P3HT. Similarly, the value of R_g of the PCBM aggregates for the annealed films of different PCBM loading can be extracted; these values show, however, a limited growth, from 18 to 22 nm, upon increasing the PCBM loading from 38 to 55% (see Figure S3 in the Supporting Information). Because these PCBM aggregates had such significantly large sizes and number densities (proportional to the loading percentage), it was inevitable that the PCBM aggregates would affect the dimensions and orientations of the P3HT
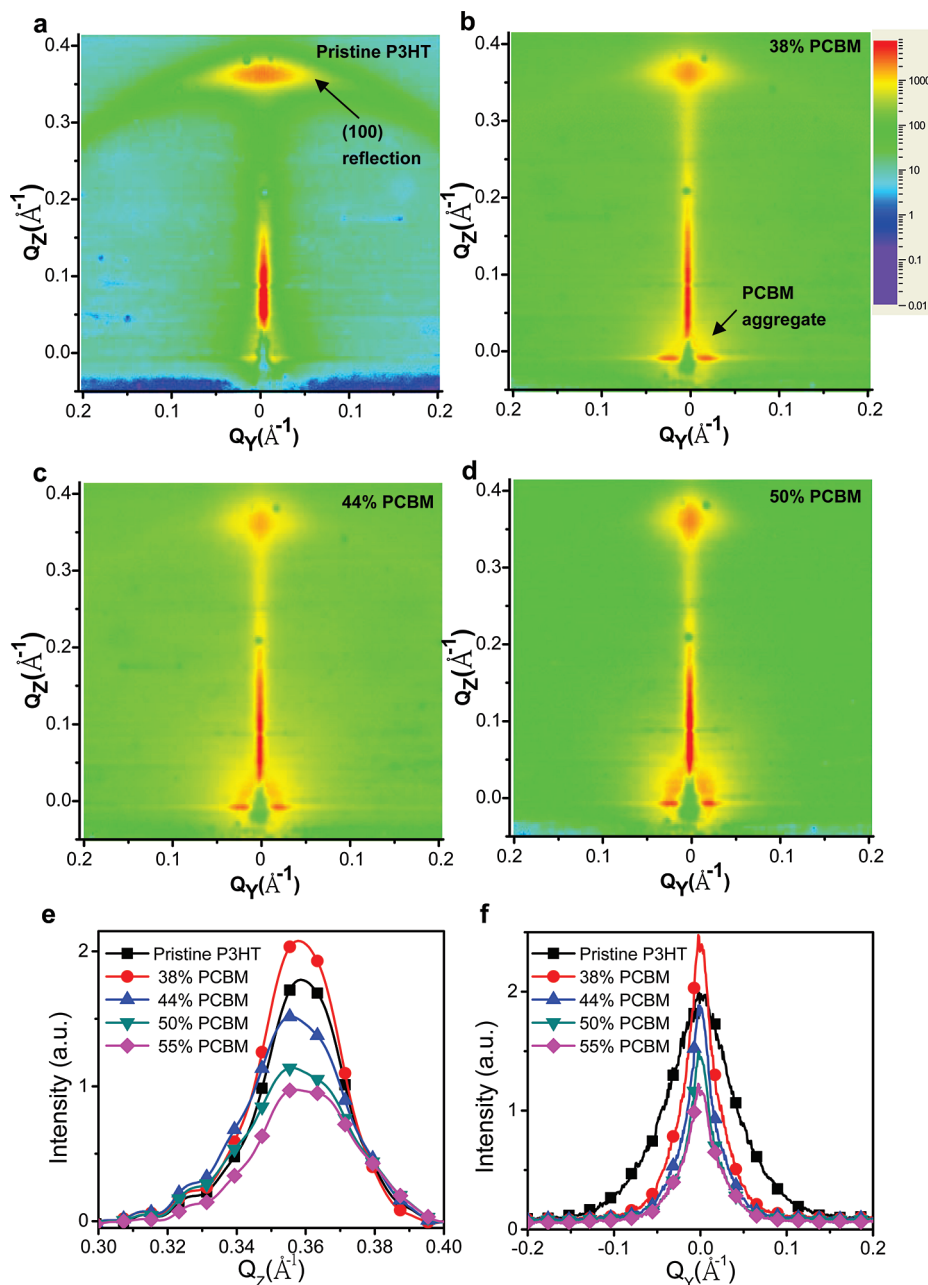
Figure 2. GISAXS patterns of the P3HT film (a), and the P3HT/PCBM films with 38% (b), 44% (c), and 50% (d) of PCBM. GISAXS profiles taken along $Q_Y = 0$ (e) and $Q_Z = 0.36$ Å^{-1} (f) for the P3HT 100 reflection.
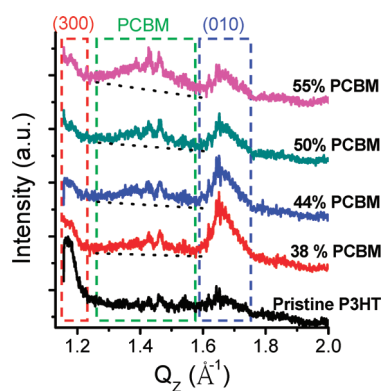

Figure 3. GIWAXD profiles of pristine P3HT and P3HT/PCBM thin films, with the respective contributions indicated.

crystallites in the thin films, as illustrated above. The PCBM aggregates (50−60 nm as estimated from the R_g value, assuming a globular shape) were substantially larger than the P3HT crystallites (ca. 20 nm) and remained so for PCBM contents within the range from 38 to 50 wt % [i.e., P3HT:PCBM ratios from 1:0.6 to 1:1 (w:w)]. Very likely, the PCBM aggregates underwent partitioning, thereby confining the P3HT crystallites, leading to smaller domain sizes in the out-of-plane direction and improved ordering in the in-plane direction as the plane of the thiophene rings in P3HT obtained better support from the PCBM aggregates (acting as partition walls).

Figure 4b displays the out-of-plane hole mobilities (μ_h) and electron mobilities (μ_e) of the P3HT/PCBM thin films, determined from devices having the structure indium tin oxide (ITO)/poly(3,4-ethylenedioxythiophene) (PEDOT)/active layer/Au and Ag/active layer/Al, and fitted using the space-charge-limited current (SCLC) model.[34−36] For the thin film incorporating
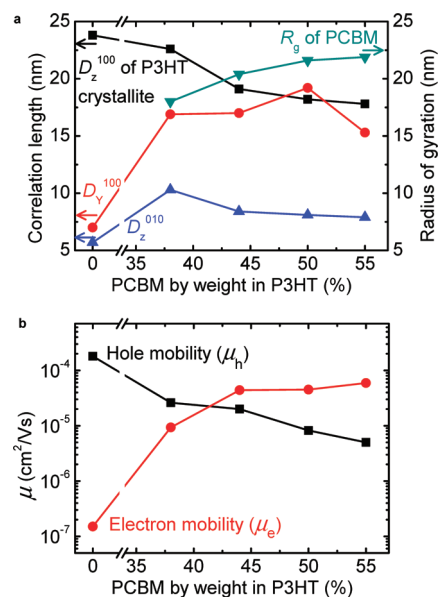
Figure 4. Dimensions of P3HT crystallites in the presence of PCBM and the corresponding charge mobilities: (a) correlation lengths of P3HT crystallites at various planes and values of R_g of PCBM; (b) hole/electron mobilities in the P3HT/PCBM films, determined using the SCLC model.
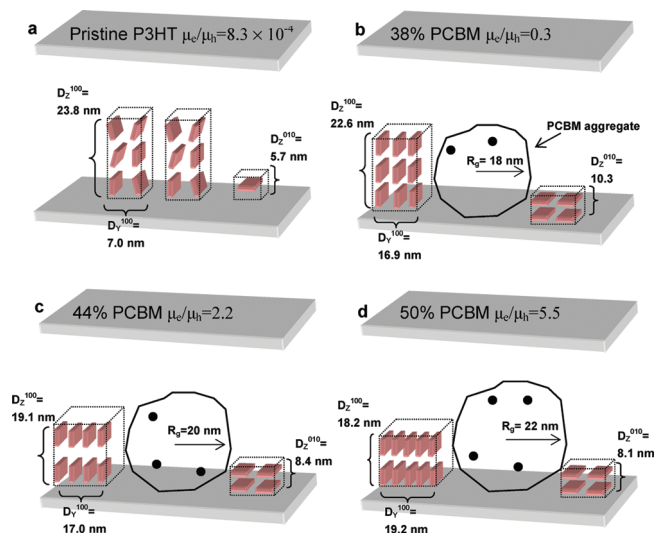

Figure 5. Schematic representation of the overall thin film P3HT/PCBM morphology. (a) Pristine P3HT: a longer out-of-plane correlation length of the (100) plane of P3HT crystallites. (b) 38% PCBM device: PCBM aggregates partition the P3HT crystallite domains that slightly reduces the (100) correlation in the z direction, and facilitate ordering in the (010) plane of the P3HT crystallites. (c) 44% PCBM device: the balance morphology, with D_Z^{100} = 19.1 nm and D_Y^{100} = 17.0 nm for the P3HT crystallites and R_g = 20 nm for the PCBM aggregates. (d) 50% PCBM device: characterized by the slightly over-suppressed P3HT crystallites due to the slightly overdosed PCBM aggregates (resulting in a biased μ_e/μ_h value for the decreased power conversion efficiency shown in Table 1). Not drawn to scale.

38% PCBM in P3HT, the value of μ_h decreased to 2.6×10^{-5} cm^2 V^{-1} s^{-1} from that of 1.8×10^{-4} cm^2 V^{-1} s^{-1} for the pristine P3HT film. The decrease in the value of the out-of-plane μ_h upon increasing the PCBM loading can be explained by considering that (i) the out-of-plane correlation length, D_Z^{100}, of the P3HT crystallites decreased from 23.8 to 17.8 nm, (ii) more P3HT lamellae were oriented in the (010) plane, which had a much shorter correlation length (D_Z^{010} < 10 nm), and (iii) a shorter

Table 1. Device Electronic Parameters Measured at Various P3HT/PCBM Blend Ratios, after Annealing at 150 °C for 15 min

% PCBM by weight in P3HT	V_{oc} (V)	J_{sc} (mA cm^{-2})	FF (%)	PCE (%)
38 (1:0.6);	0.65	−9.03	52	3.06
44 (1:0.8);	0.65	−9.35	61	3.70
50 (1:1);	0.65	−8.66	58	3.28
55 (1:1.2);	0.65	−7.87	55	2.80

pathway for hole transport arose because of the large number of PCBM aggregates that intercalated between the P3HT domains. The extent of the contribution from each of these factors remains unclear at present.

For the system featuring 38% PCBM loaded in P3HT, the value of μ_e of the film increased to 9.3×10^{-6} cm^2 V^{-1} s^{-1} from that of 1.5×10^{-7} cm^2 V^{-1} s^{-1} for pristine P3HT. For PCBM loadings from 38 to 50%, the increase in μ_e was due presumably to the improved quality of the percolated network (i.e., higher number density of PCBM aggregates) for electron transport, despite the size of the PCBM aggregates (R_g) remaining approximately constant (from 18 to 22 nm). Thus, we conclude that hole transport in the thin films was governed simultaneously by the out-of-plane correlation length, the (010) plane of the P3HT crystallites, and the number density (weight percentage) of the P3HT crystallites. In contrast, electron transport in these thin films was determined by the sizes and number densities of the PCBM aggregates (i.e., the effects of annealing and the PCBM concentration). Parts a−d of Figure 5 summarize the overall morphologies and related characteristic length scales of the P3HT/PCBM thin films, as extracted from the results of our GISAXS and GIWAXD analyses.

Table 1 summarizes the open-circuit voltages (V_{oc}), short-circuit current densities (J_{sc}), filling factors (FFs), and PCEs of our BHJ solar cells illuminated at 100 mW cm^{-2} under AM1.5G. The highest PCE (3.7%) and the lowest μ_e/μ_h ratio (2.2) occurred at a PCBM loading of 44% as a result of the improved values of J_{sc} and FF.[8]

Our composition-dependent morphological study result is consistent with conclusions in previous reports[27,37] that both the crystallization of P3HT chains and aggregation of PCBM coexist at the optimum PCBM concentration in the blend, and the optimum PCBM concentration falls into the range between 40 and 50 wt % when the thickness of the active layer is between 90 to 140 nm.

Conclusions

We have used simultaneous GISAXS and GIWAXD to elucidate the morphologies of locally phase-separated P3HT crystallites intercalated with the relatively large PCBM aggregates in the composite thin films for BHJ solar cells. The optimal performance of the composite film occurred at an appropriate size and number density (concentration) of the PCBM aggregates. At balanced levels of the P3HT crystallites and PCBM aggregates, highly interpercolated networks formed provide balanced charge and hole transport routes in the BHJ thin films, thereby resulting in more efficient solar cells.

Supporting Information Available: Text and figures giving further experimental details of the Guinier approximation and results, SCLC model and dark J−V curves, profiles of azimuthal

Chiu et al.

angles, and current density−voltage characteristics of solar cells used in this work. This material is available free of charge via the Internet at http://pubs.acs.org.

References and Notes

(1) Sirringhaus, H.; Brown, P. J.; Friend, R. H.; Nielsen, M. M.; Bechgaard, K.; Langeveld-Voss, B. M. W.; Spiering, A. J. H.; Janssen, R. A. J.; Meijer, E. W.; Herwig, P.; de Leeuw, D. M. *Nature* **1999**, *401*, 685–688.

(2) Kline, R. J.; McGehee, M. D.; Kadnikova, E. N.; Liu, J.; Frechet, J. M. J.; Toney, M. F. *Macromolecules* **2005**, *38*, 3312–3319.

(3) Yu, G.; Gao, J.; Hummelen, J. C.; Wudl, F.; Heeger, A. J. *Science* **1995**, *270*, 1789–1791.

(4) Huynh, W. U.; Dittmer, J. J.; Alivisatos, A. P. *Science* **2002**, *295*, 2425–2427.

(5) Yang, X.; Loos, J. *Macromolecules* **2007**, *40*, 1353–1362.

(6) Zhang, Q.; Russell, T. P.; Emrick, T. *Chem. Mater*. **2007**, *19*, 3712–3716.

(7) Ma, W.; Yang, C.; Gong, X.; Lee, K.; Heeger, A. J. *Adv. Funct. Mater*. **2005**, *15*, 1617–1622.

(8) Li, G.; Shrotriya, V.; Huang, J.; Yao, Y.; Moriarty, T.; Emery, K.; Yang, Y. *Nat. Mater*. **2005**, *4*, 864–868.

(9) Reyes-Reyes, M.; Kim, K.; Carroll, D. L. *Appl. Phys. Lett*. **2005**, *87*, 083506.

(10) Peet, J.; Kim, J. Y.; Coates, N. E.; Ma, W. L.; Moses, D.; Heeger, A. J.; Bazan, G. C. *Nat. Mater*. **2007**, *6*, 497–500.

(11) Chang, Y. T.; Hsu, S. L.; Su, M. H.; Wei, K. H. *Adv. Mater*. **2009**, *21*, 2093–2097.

(12) Liang, Y.; Wu, Y.; Feng, D.; Tsai, S. T.; Son, H. J.; Li, G.; Yu, L. *J. Am. Chem. Soc*. **2009**, *131*, 56–57.

(13) Hou, J.; Chen, H. Y.; Zhang, S.; Li, G.; Yang, Y. *J. Am. Chem. Soc*. **2008**, *130*, 16144–16145.

(14) Park, S. H.; Roy, A.; Beaupre, S.; Cho, S.; Coates, N.; Moon, J. S.; Moses, D.; Leclerc, M.; Lee, K.; Heeger, A. J. *Nat. Photon*. **2009**, *3*, 297–303.

(15) Wienk, M. M.; Turbiez, M.; Gilot, J.; Janssen, R. A. J. *Adv. Mater*. **2008**, *20*, 2556–2560.

(16) Zhu, Z.; Waller, D.; Gaudiana, R.; Morana, M.; Muhlbacher, D.; Scharber, M.; Brabec, C. *Macromolecules* **2007**, *40*, 1981–1986.

(17) Hou, L.; Hou, J.; Chen, H. Y.; Zhang, S.; Jiang, Y.; Chen, T. L.; Yang, Y. *Macromolecules* **2009**, *42*, 6564–6571.

(18) Kim, Y.; Cook, S.; Tuladhar, S. M.; Choulis, S. A.; Nelson, J.; Durrant, J. R.; Bradley, D. D. C.; Giles, M.; Mcculloch, I.; Ha, C. S.; Ree, M. *Nat. Mater*. **2006**, *5*, 197–203.

(19) Erb, T.; Zhokhavets, U.; Gobsch, G.; Raleva, S.; Stuhn, B.; Schilinsky, P.; Waldauf, C.; Brabec, C. J. *Adv. Funct. Mater*. **2005**, *15*, 1193–1196.

(20) Woo, C. H.; Thompson, B. C.; Kim, B. J.; Toney, M. F.; Frechet, J. M. J. *J. Am. Chem. Soc*. **2009**, *130*, 16324–16329.

(21) Chu, C. W.; Yang, H.; Hou, W. J.; Hunag, J.; Li, G.; Yang, Y. *Appl. Phys. Lett*. **2008**, *92*, 103306.

(22) Li, G.; Yao, Y.; Yang, H.; Shrotriya, V.; Yang, G.; Yang, Y. *Adv. Funct. Mater*. **2007**, *17*, 1636–1644.

(23) Chen, H. Y.; Yang, H.; Yang, G.; Sista, S.; Zadoyan, R.; Li, G.; Yang, Y. *J. Phys. Chem. C* **2009**, *113*, 7946–7953.

(24) Yang, X.; Loos, J.; Veenstra, S. C.; Verhees, W. J. H.; Wienk, M. M.; Kroon, J. M.; Michels, M. A. J.; Janssen, R. A. J. *Nano Lett*. **2005**, *5*, 579–583.

(25) Ma, W.; Yang, C.; Heeger, A. J. *Adv. Mater*. **2007**, *19*, 1387–1390.

(26) van Bavel, S. S.; Sourty, E.; de With, G.; Loos, J. *Nano Lett*. **2009**, *9*, 507–513.

(27) Campoy-Quiles, M.; Ferenczi, T.; Agostinelli, T.; Etchegoin, P. G.; Kim, Y.; Anthopoulos, T. D.; Stavrinou, P. N.; Bradley, D. D. C.; Nelson, J. *Nat. Mater*. **2008**, *7*, 158–164.

(28) Klimov, E.; Li, W.; Yang, X.; Hoffmann, G. G.; Loos, J. *Macromolecules* **2006**, *39*, 4493–4496.

(29) Xu, Z.; Chen, L. M.; Yang, G.; Huang, C. H.; Hou, J.; Wu, Y.; Li, G.; Hsu, C. S.; Yang, Y. *Adv. Funct. Mater*. **2009**, *19*, 1227–1234.

(30) Chiu, M. Y.; Jeng, U. S.; Su, C. H.; Liang, K. S.; Wei, K. H. *Adv. Mater*. **2008**, *20*, 2573–2578.

(31) Jeng, U.; Su, C. H.; Su, C. J.; Liao, K. F.; Chuang, W. T.; Lai, Y. H.; Chang, J. W.; Chen, Y. J.; Huang, Y. S.; Lee, M. T.; Yu, K. L.; Lin, J. M.; Liu, D. G.; Chang, C. F.; Liu, C. Y.; Chang, C. H.; Liang, K. S., *J. Appl. Crystallogr*., in press.

(32) Lai, Y. H.; Sun, Y. S.; Jeng, U.; Lin, J. M.; Lin, T. L.; Sheu, H. S.; Chuang, W. T.; Huang, Y. S.; Hsu, C. H.; Lee, M. T.; Lee, H. Y.; Liang, K. S.; Gabriel, A.; Koch, M. H. J. *J. Appl. Crystallogr*. **2006**, *39*, 871–877.

(33) Prosa, T. J.; Winokur, M. J.; Moulton, J.; Smith, P.; Heeger, A. J. *Macromolecules* **1992**, *25*, 4364–4372.

(34) Melzer, C.; Koop, E. J.; Mihailetchi, V. D.; Blom, P. W. M. *Adv. Funct. Mater*. **2004**, *14*, 865–870.

(35) Mihailetchi, V. D.; Xie, H.; de Boer, B.; Koster, L. J. A.; Blom, P. W. M. *Adv. Funct. Mater*. **2006**, *16*, 699–708.

(36) Mihailetchi, V. D.; Wildeman, J.; Blom, P. W. M. *Phys. Rev. Lett*. **2005**, *94*, 126602–4.

(37) Müller, C.; Ferenczi, T. A. M.; Campoy-Quiles, M.; Frost, J. M.; Bradley, D. D. C.; Smith, P.; Stingelin-Stutzmann, N.; Nelson, J. *Adv. Mater*. **2008**, *20*, 3510–3515.